Regular Article – Experimental Physics

# Investigation of the influence of incomplete fusion on complete fusion of $^{12}$C-induced reactions at $\approx$ 4–7.2 MeV/nucleon

F.K. Amanuel[1,a], B. Zelalem[2], A.K. Chaubey[2], Avinash Agarwal[3], I.A. Rizvi[4], Anjana Maheshwari[4], and Tauseef Ahmed[4]

[1] INFN, Laboratori Nazionali di Legnaro, Legnaro (Padova), Italy
[2] Department of Physics, Addis Ababa University, P.O.Box 1176, Addis Ababa, Ethiopia
[3] Department of Physics, Bareilly College, Bareilly, 243005, India
[4] Department of Physics, Aligarh Muslim University, Aligarh, 202002, India

**Abstract.** In this paper, we present the results of our investigation of reaction dynamics leading to incomplete fusion of heavy ions at moderate excitation energies, especially the influence of incomplete fusion on complete fusion of $^{12}$C-induced reactions at specific energies $\approx$ 4–7.2 MeV/nucleon. Excitation functions of various reaction products populated via complete and/or incomplete fusions of a $^{12}$C projectile with $^{93}$Nb, $^{59}$Co and $^{52}$Cr targets were measured at several specific energies $\approx$ 4–7.2 MeV/nucleon, using a recoil catcher technique, followed by off-line $\gamma$-ray spectrometry. The measured excitation functions were compared with theoretical values obtained using the PACE4 statistical model code. For representative non–$\alpha$-emitting channels in the $^{12}$C + $^{93}$Nb system, the experimentally measured excitation functions were, in general, found to be in good agreement with the theoretical predictions. However, for $\alpha$-emitting channels in the $^{12}$C + $^{93}$Nb, $^{12}$C + $^{59}$Co, and $^{12}$C + $^{52}$Cr systems, the measured excitation functions were higher than the predictions of the theoretical model code, which may be credited to incomplete fusion reactions at these energies. An attempt was made to estimate the incomplete fusion fraction for the present systems, which revealed that the fraction was sensitive to the projectile energy and mass asymmetry of the entrance channel.

## 1 Introduction

During the past few years the role of incomplete fusion (ICF) in light-heavy-ion–induced reactions at low projectile energies has been a subject of renewed interest, especially after it was observed that ICF start competing with complete fusion (CF) reactions just above the Coulomb barrier [1–3]. Recent studies report that not only are both CF and ICF reactions possible at these energies, but they are in fact the most dominant reaction mechanisms [4–7].

Recently, it has been observed that ICF becomes more and more dominant as the projectile energy increases a little above the Coulomb barrier ($V_{CB}$) [8–12]. It is now known that CF occurs where the angular momentum imparted to the system is less than or equal to $l_{crit}$ [13]. In sharp cut-off approximation the probability of CF is assumed to be unity until $l \approx l_{crit}$ and expected to be zero for $l > l_{crit}$ [14,15]; while at relatively higher projectile energies and at finite values of impact parameters, CF gradually gives way to ICF, where fractional mass and charge as well as the linear momentum of the projectile are transferred to the target nucleus due to prompt emission of $\alpha$-clusters in the forward cone with almost projectile velocity. As a result of such processes, projectile-like and target-like partners may come into the picture in the exit channel. Such reaction processes were first observed by Britt and Quinton [16] in the bombardment of heavy targets by $^{12}$C, $^{14}$N, and $^{16}$O projectiles at energies well above the Coulomb barrier. Further, particle-$\gamma$ coincidence studies by Inamura *et al.* [17] contributed a great deal to the understanding of the underlying reaction dynamics. The most common features of ICF reactions are:

i) the outgoing particles have forward peaked angular distribution and energy spectrum peaked at beam velocity [17];

ii) the recoil range distribution of heavy residues shows a low range of components, suggesting incomplete momentum transfer;

iii) the spin distribution of evaporation residues populated via ICF are found to be distinctly different from those of CF [17,18].

a e-mail: kifle@lnl.infn.it

Several dynamical models have been proposed to explain the mechanism of ICF reactions. The Breakup Fusion model of Tamura and Udagawa [19] explained ICF in terms of the breakup of the projectile in the nuclear force field of the target nucleus followed by the fusion of one of the fragments with the target. The model uses the distorted wave Born approximation to evaluate the shapes of the energy spectra and the angular distributions of projectile-like fragments but does not give absolute cross-sections, due to the lack of information about the spectroscopic form factors of the continuum states of the product nuclei. The Sum Rule model of Wilczynski *et al.* [20] assumes that the various ICF channels are localized in the angular momentum space above the critical angular momentum for a CF of the projectile and target. The model gives cross-sections for reaction products arising not only from ICF and quasi-elastic transfer reactions but also from CF. Other dynamical models, like the Exciton model [21], the Hot Spot model [22], the Promptly Emitted Particles model [23], and the Multistep Direct Reaction model [24] have also been proposed to explain ICF dynamics. Morgenstern *et al.* [25,26] investigated the mass-asymmetry dependence of the ICF contribution. The details of the above models are given in ref. [27].

Reasonably, studies on ICF were confined to beam energies greater than 10 MeV/nucleon. However, none of the proposed models is able to reproduce the experimental data obtained at energies as low as $\approx 4$–8 MeV/nucleon.

Recent experiments have shown significant ICF contributions even at energies just above the fusion barrier [5,28,29]. These findings have motivated many to investigate ICF at relatively low bombarding energies. However, a clear and robust modeling of ICF processes is still lacking, especially at relatively low bombarding energies ($\approx 4$–8 MeV/nucleon), where a clear systematic study and compiled data are available for only a few projectile-target systems. In view of this, in the present work, the influence of ICF on CF was studied for $^{12}$C + $^{93}$Nb, $^{12}$C + $^{59}$Co, and $^{12}$C + $^{52}$Cr systems at energies $\approx 4$–7.2 MeV/nucleon. This work follows our earlier observations and the publications of a part of our analysis on $^{12}$C + $^{59}$Co and $^{12}$C + $^{52}$Cr systems [30,31].

Excitation functions (EFs) for various evaporation residues produced in the interaction of the $^{12}$C + $^{53}$Nb, $^{12}$C + $^{59}$Co, and $^{12}$C + $^{52}$Cr systems were measured at various projectile energies ranging from $\approx 45$ MeV to 87 MeV for reaction products that may be populated via CF and/or ICF processes using the thick target-catcher technique. It may be pointed out that the charge products ($Z_1 \cdot Z_2 \leq 246$) of the present systems are far less than 1600 and, therefore, the probability of possible fission reactions is negligible [32]. Results of the present work may also provide a new cross-section data base for several residues produced in the reaction. Further, in this work, an attempt was made to estimate the ICF fraction of the measured production cross-sections.

In sect. 2, experimental procedures and results are briefed; in the sections to follow the measured EFs are compared with the theoretical model predictions and the results of the present analysis are also presented. A de-
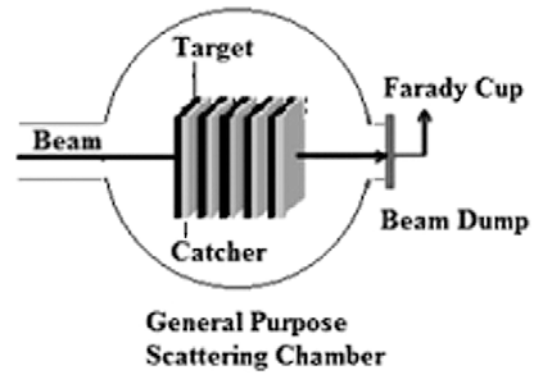


**Fig. 1.** Typical experimental setup for EFs measurement using the Energy Degradation Technique.

tailed discussion of the influence of ICF fraction, calculated on the lines of Gomes *et al.*, [33], is given in sect. 5. The last section deals with the summary and conclusions of the present work.

## 2 Experimental procedure

The experiment was carried out at the Inter-University Accelerator Center (IUAC), New Delhi (India) using a general purpose scattering chamber (GPSC), which has an in-vacuum transfer of targets facility so that the time lapse between stopping of irradiation and beginning of counting can be minimized. A stack containing five samples of $^{93}$Nb, sandwiched between five Al catchers, was irradiated at beam energy $\approx 74$ MeV, while, a stack of five $^{59}$Co samples and a stack of six $^{52}$Cr samples, sandwiched between five and six Al catchers, were irradiated at beam energy $\approx 80$ MeV and $\approx 86.4$ MeV, respectively, by a $^{12}$C$^{5+/6+}$ beam in the GPSC. A typical stacked foil (five targets + five catchers) arrangement used for excitation function measurements is shown in fig. 1. The irradiation of the three stacks covered the desired energy range of $\approx 45$–87 MeV for measuring the EFs of various evaporation residues produced in the $^{12}$C + $^{93}$Nb, $^{12}$C + $^{59}$Co, and $^{12}$C + $^{52}$Cr systems. The beam currents were $\approx 25$–40 pnA for the three systems throughout the irradiations. $^{52}$Cr targets of thickness $\approx 364 \, \mu$g/cm$^2$, $^{59}$Co and $^{93}$Nb targets of thickness $\approx 350 \, \mu$g/cm$^2$ and 2.02 mg/cm$^2$, respectively, backed by Al catchers of appropriate thickness ($\approx 2$–2.08 mg/cm$^2$), were placed after each target normal to the beam direction so that the recoiling nuclei coming out of the targets may be trapped in the catcher foil and there would be no loss of activity. To ensure more efficient collection of CF and ICF products, the thickness of Al backings was carefully chosen.

The incident flux of the $^{12}$C beam was determined from the charge collected in Faraday Cup (using an ORTEC current integrator device), as well as from the counts of the two Rutherford monitors kept at $\pm 10°$ to the beam direction. The two sets of values were found to agree, and their corresponding values were within 5% of each other.

**Table 1.** Decay characteristics of nuclides studied in the $^{12}$C + $^{93}$Nb system.

| Reaction | Nuclide | Half-life | $\gamma$-ray energy (keV) | $I_\gamma$ $\gamma$/decay |
|---|---|---|---|---|
| $^{93}$Nb($^{12}$C, $\alpha$n) | $^{100}$Rh | 20.8 h | 539 | 0.784 |
| $^{93}$Nb($^{12}$C, $\alpha$3n) | $^{98}$Rh | 8.7 m | 652 | 0.96 |
| $^{93}$Nb($^{12}$C, $\alpha$p3n) | $^{97}$Ru | 2.9 d | 215.72 | 0.86 |
| $^{93}$Nb($^{12}$C, 2$\alpha$n) | $^{96}$Tc | 4.28 d | 778.22, 849.92, 812.58 | 1, 0.98, 0.82 |
| $^{93}$Nb($^{12}$C, 2$\alpha$2n) | $^{95}$Tc | 20 h, 61 d | 765.79, 204.11 | 0.938, 0.632 |
| $^{93}$Nb($^{12}$C, 2$\alpha$3n) | $^{94}$Tc | 293 m | 871.09, 702.62 | 1, 0.996 |
| $^{93}$Nb($^{12}$C, $\alpha$p3n) | $^{93}$Mo | 6.85 h | 1477.13, 684.67, 263.06 | 0.991, 0.997, 0.567 |

**Table 2.** Decay characteristics of nuclides studied in the $^{12}$C + $^{59}$Co system.

| Reaction | Nuclide | Half-life | $\gamma$-ray energy (keV) | $I_\gamma$ $\gamma$/decay |
|---|---|---|---|---|
| $^{59}$Co($^{12}$C, $\alpha$n) | $^{66}$Ga | 9.49 h | 1039.4, 833.6 | 0.379, 0.0603 |
| $^{59}$Co($^{12}$C, $\alpha$2n) | $^{65}$Ga | 15.2 m | 115.2, 61.2, 153.1, 751.9 | 0.55, 0.116, 0.09, 0.082 |
| $^{59}$Co($^{12}$C, $\alpha$p3n) | $^{63}$Zn | 38.1 m | 669.8, 962.2 | 0.084, 0.066 |
| $^{59}$Co($^{12}$C, 2$\alpha$2n) | $^{61}$Cu | 3.41 h | 67.4, 282.9, 656 | 0.0394, 0.125, 0.1066 |

**Table 3.** Decay characteristics of nuclides studied in the $^{12}$C + $^{52}$Cr system.

| Reaction | Nuclide | Half-life | $\gamma$-ray energy (keV) | $I_\gamma$ $\gamma$/decay |
|---|---|---|---|---|
| $^{52}$Cr($^{12}$C, $\alpha$3n) | $^{57}$Ni | 1.50 d | 1377.6, 1919.5 | 0.779, 0.147 |
| $^{52}$Cr($^{12}$C, $\alpha$4n) | $^{56}$Ni | 6.10 d | 158.4, 811.9 | 0.988, 0.86 |
| $^{52}$Cr($^{12}$C, $\alpha$pn) | $^{58}$Co | 70.91 d | 810.8 | 0.995 |
| $^{52}$Cr($^{12}$C, $\alpha$p2n) | $^{57}$Co | 271.77 d | 122.06 | 0.855 |
| $^{52}$Cr($^{12}$C, $\alpha$p3n) | $^{56}$Co | 77.70 d | 846.8 | 0.999 |

The stacks were irradiated for $\approx$ 3–6.5 h, keeping in mind the half-lives of interest.

The energy of the $^{12}$C ion beam that impinges at each target foil in the stacks was calculated from the energy degradation of the initial beam energy using the Stopping Power and Range of Ions in Matter (SRIM) software [34]. The energy values corresponding to each cross-section point in the measured EFs refer to the middle of the targets. In these calculations energy straggling was neglected due to its small contribution [35].

The activities induced in the target-catcher assembly were followed off-line, using a pre-calibrated CANBERA's HPGe detector coupled to a PC through CAMAC and based on an IUAC developed FREEDOM data acquisition system [36]. The average time between the end of the irradiation and the beginning of the measurements with HPGe was $\approx$ 3–7 min.

The nuclear spectroscopic data used in the evaluations and measurements of cross-sections were adopted from the radioactive isotopes data Table of Browne and Firestone's [37] and are given in tables 1–3.

The spectrometer was calibrated for energy and efficiency was measured using various standard sources, *i.e.* $^{152}$Eu, $^{60}$C, $^{57}$Co and $^{133}$Ba. Details of geometry dependent efficiency measurements used in this work are similar to those used by Gupta *et al.* [3]. The residues produced from various reaction channels were identified by their characteristic $\gamma$-ray and decay-curve analysis.

The following energy-dependent standard expression was used for computing the experimentally measured reaction cross-sections [38]

$$\sigma = \frac{A\lambda \exp(\lambda t_2)}{\phi N_0 \varepsilon \cdot G \theta K [1 - \exp(-\lambda t_1)][1 - \exp(-\lambda t_3)]}, \quad (1)$$

where $A$ is the total number of counts in the photo peak of the characteristic $\gamma$-ray, $\lambda$ is the decay constant of the product nucleus, $N_0$ is the number of nuclei of the isotope under investigation, $\phi$ is the incident flux, $\varepsilon G$ is the geometry dependent efficiency of the HPGe detector, $\theta$ is the absolute intensity of the characteristic $\gamma$-ray, $K = \frac{(1 - \exp(-\mu d))}{\mu d}$ is the self-absorption correction factor

**Table 4.** Experimentally measured cross-sections in mb for residues populated via $\alpha$-emitting channels in the $^{12}$C + $^{93}$Nb system.

| $E_{proj}$(MeV) | $^{100}$Rh | $^{98}$Rh | $^{97}$Ru | $^{96}$Tc | $^{95}$Tc | $^{94}$Tc | $^{93}$Mo |
|---|---|---|---|---|---|---|---|
| $47.0 \pm 1.1$ | $45.1 \pm 4.9$ | $6.2 \pm 1.1$ | – | – | – | $2.1 \pm 0.3$ | – |
| $54.0 \pm 1.3$ | $26.8 \pm 9.2$ | $76.9 \pm 16.9$ | – | $23.8 \pm 3.6$ | $181.8 \pm 27.3$ | $28 \pm 4.2$ | $2.4 \pm 0.4$ |
| $62.0 \pm 1.2$ | $9.8 \pm 2.4$ | $908.6 \pm 199.8$ | – | $75.7 \pm 11.4$ | $42.7 \pm 6.4$ | $42.4 \pm 6.4$ | $3.5 \pm 0.5$ |
| $68.0 \pm 1.1$ | $46.6 \pm 11.6$ | $2997.8 \pm 719.9$ | $34.3 \pm 5.1$ | $98.9 \pm 3.8$ | $631.8 \pm 94.8$ | $67.6 \pm 10.1$ | $6.2 \pm 0.9$ |
| $74.0 \pm 0.9$ | $74.1 \pm 18.5$ | $2665.5 \pm 639.7$ | $7.5 \pm 14.6$ | $101.0 \pm 15.2$ | $672.7 \pm 101.0$ | $78.4 \pm 11.8$ | $8.4 \pm 1.3$ |

**Table 5.** Experimentally measured cross-sections in mb for residues populated via $\alpha$-emitting channels in the $^{12}$C + $^{59}$Co system.

| $E_{proj}$(MeV) | $^{66}$Ga | $^{65}$Ga | $^{63}$Zn | $^{61}$Cu |
|---|---|---|---|---|
| $60.0 \pm 1.3$ | $62.2 \pm 14.9$ | $134.8 \pm 32.1$ | – | $28.1 \pm 6.7$ |
| $65.0 \pm 1.2$ | $72.0 \pm 17.3$ | $169.9 \pm 40.8$ | – | $57.1 \pm 13.7$ |
| $70.0 \pm 1.1$ | $108.8 \pm 26.1$ | $98.8 \pm 23.7$ | – | $95.3 \pm 22.9$ |
| $75.0 \pm 1.1$ | $214.8 \pm 51.5$ | $94.5 \pm 22.7$ | $180.4 \pm 33.3$ | $218.3 \pm 52.3$ |
| $80.0 \pm 0.9$ | $473.2 \pm 113.6$ | $83.3 \pm 20.0$ | $126.6 \pm 30.4$ | $635.5 \pm 152.5$ |

**Table 6.** Experimentally measured cross-sections (cumulative (cuml)/deduced independent (ind), if any) in mb for residues populated via $\alpha$-emitting channels in the $^{12}$C + $^{52}$Cr system.

| $E_{proj}$(MeV) | $^{56}$Ni | $^{57}$Ni | $^{58}$Co | $^{57}$Co (ind) | $^{57}$Co (cuml) | $^{56}$Co (ind) | $^{56}$Co (cuml) |
|---|---|---|---|---|---|---|---|
| $51.5 \pm 1.1$ | – | $27.1 \pm 4.6$ | $317.9 \pm 54.0$ | $97.8 \pm 16.6$ | $97.8 \pm 16.6$ | – | – |
| $60.0 \pm 0.9$ | – | $79.5 \pm 13.5$ | $278.8 \pm 47.4$ | $343.4 \pm 58.4$ | $343.4 \pm 58.4$ | – | – |
| $67.3 \pm 1.6$ | – | $113.8 \pm 19.4$ | $165.8 \pm 28.2$ | $598.8 \pm 101.3$ | $598.8 \pm 101.3$ | $86.5 \pm 14.7$ | $86.5 \pm 14.7$ |
| $74.1 \pm 1.0$ | $26.9 \pm 4.6$ | $128.3 \pm 21.8$ | $87.8 \pm 14.9$ | $607.0 \pm 108.4$ | $637.0 \pm 108.3$ | $79.2 \pm 41.6$ | $208.3 \pm 35.4$ |
| $79.5 \pm 0.9$ | $44.4 \pm 7.5$ | $131.7 \pm 22.4$ | $69.9 \pm 11.8$ | $486.1 \pm 91.2$ | $534.3 \pm 90.8$ | $341.0 \pm 83.6$ | $473.5 \pm 80.5$ |
| $86.4 \pm 1.5$ | $55.5 \pm 9.4$ | $104.5 \pm 17.8$ | $112.8 \pm 19.2$ | $318.5 \pm 65.2$ | $378.7 \pm 64.4$ | $582.3 \pm 118.2$ | $687.4 \pm 116.8$ |

for the material of the sample, of thickness $d$, absorption coefficient $\mu$, $t_1$ is the irradiation time of the target-catcher assembly, $t_2$ is the time elapsed between the end of the irradiation and the start of counting and $t_3$ is the accumulation time. The correction factor for the decay of the induced activity due to the delay time $t_2$ is taken as $[\exp(-\lambda t_2)]$ and the correction factor due to the decay of the irradiated sample during $t_3$ is taken as $[1-\exp(-\lambda t_3)]$. $[1 - \exp(-\lambda t_1)]$ is a saturation correction factor.

The standard formulation mentioned above was used to determine the production cross-sections of various reaction products. Details of the experimental arrangements and data reduction procedures are given in ref. [30]. The errors in the measured production cross-sections may arise mainly because of the non-uniform thickness of the samples, which may lead to uncertainty in the determination of the number of target nuclei. Fluctuations in the beam current may result in a variation of the incident flux. Proper care was taken to keep the beam current constant as far as possible and, a correction was applied to account for the fluctuation in the beam current and the consequent variation in incident flux. Uncertainty in the determination of geometry-dependent spectrometer effi-

ciency is another cause of error. Product nuclei recoiling out of the sample may introduce significant errors in the measured cross-sections. The dead time in the spectrometer may lead to a loss in the counts. By suitably adjusting the sample-detector distance, the dead time was kept below 10%. These errors excluded uncertainty of the nuclear data, such as branching ratio, decay constant, etc., which have been taken from the table of isotopes. Attempts were made to minimize the uncertainties caused by all the above possible factors. The overall error in the present work is estimated to be between $\approx$ 17–26%.

The experimentally measured cross-sections for the production of various residues populated via $\alpha$-emitting ($\alpha$-emit) channels in the $^{12}$C + $^{93}$Nb, $^{12}$C + $^{59}$Co and $^{12}$C + $^{52}$Cr systems are given in tables 4–6, respectively.

# 3 Results and analysis

EFs for residues produced in the $^{12}$C + $^{52}$Cr, $^{12}$C + $^{59}$Co, and $^{12}$C + $^{93}$Nb systems via CF and/or ICF processes were measured at projectile energies up to 87 MeV. To investigate the ICF reaction dynamics, the EFs for residues

**Table 7.** Columns with beam energy, Bass fusion cross-section, Bass fusion barrier and radius, yrast spin at maximum excitation energy, $L$-diffuseness, $L$ at grazing, and fission barrier for $^{12}C + ^{93}Nb$ system.

| $E_{proj}$(MeV) | Bass fusion cross-section | Fusion radius, fusion barrier | Yrast spin | Diffuseness $(\Delta)$ | $l_{max}$ | Fission barrier |
|---|---|---|---|---|---|---|
| $47.0 \pm 1.1$ | 551 mb | 9.45 fm, 33.39 MeV | $53\hbar$ | $4\hbar$ | $\approx 17\hbar$ | 49.11 MeV |
| $54.0 \pm 1.3$ | 855 mb | 9.20 fm, 33.39 MeV | $57\hbar$ | $4\hbar$ | $\approx 24\hbar$ | 49.11 MeV |
| $62.0 \pm 1.2$ | 1065 mb | 8.95 fm, 33.39 MeV | $61\hbar$ | $4\hbar$ | $\approx 29\hbar$ | 49.11 MeV |
| $68.0 \pm 1.1$ | 1197 mb | 8.70 fm, 33.39 MeV | $64\hbar$ | $4\hbar$ | $\approx 33\hbar$ | 49.11 MeV |
| $74.0 \pm 0.9$ | 1286 mb | 8.40 fm, 33.39 MeV | $67\hbar$ | $4\hbar$ | $\approx 36\hbar$ | 49.11 MeV |

**Table 8.** Columns with beam energy, Bass fusion cross-section, Bass fusion barrier and radius, yrast spin at maximum excitation energy, $L$-diffuseness, $L$ at grazing, and fission barrier for $^{12}C + ^{59}Co$ system.

| $E_{proj}$ (MeV) | Bass fusion cross-section | Fusion radius, fusion barrier | Yrast spin | Diffuseness $(\Delta)$ | $l_{max}$ | Fission barrier |
|---|---|---|---|---|---|---|
| $60.0 \pm 1.3$ | 1205 mb | 7.80 fm, 23.35 MeV | $44\hbar$ | $4\hbar$ | $\approx 29\hbar$ | 51.24 MeV |
| $65.0 \pm 1.2$ | 1224 mb | 6.25 fm, 23.35 MeV | $46\hbar$ | $4\hbar$ | $\approx 30\hbar$ | 51.24 MeV |
| $70.0 \pm 1.1$ | 1224 mb | 6.25 fm, 23.35 MeV | $47\hbar$ | $4\hbar$ | $\approx 32\hbar$ | 51.24 MeV |
| $75.0 \pm 1.1$ | 1224 mb | 6.25 fm, 23.35 MeV | $49\hbar$ | $4\hbar$ | $\approx 33\hbar$ | 51.24 MeV |
| $80.0 \pm 0.9$ | 1224 mb | 6.25 fm, 23.35 MeV | $50\hbar$ | $4\hbar$ | $\approx 34\hbar$ | 51.24 MeV |

**Table 9.** Columns with beam energy, Bass fusion cross-section, Bass fusion barrier and radius, yrast spin at maximum excitation energy, $L$-diffuseness, $L$ at grazing, and fission barrier for $^{12}C + ^{52}Cr$ system.

| $E_{proj}$ (MeV) | Bass fusion cross-section | Fusion radius, fusion barrier | Yrast spin | Diffuseness $(\Delta)$ | $l_{max}$ | Fission barrier |
|---|---|---|---|---|---|---|
| $51.5 \pm 1.1$ | 1112 mb | 7.90 fm, 21.08 MeV | $39\hbar$ | $4\hbar$ | $\approx 25\hbar$ | 49.63 MeV |
| $60.0 \pm 0.9$ | 1203 mb | 6.05 fm, 21.08 MeV | $42\hbar$ | $4\hbar$ | $\approx 28\hbar$ | 49.63 MeV |
| $67.3 \pm 1.6$ | 1197 mb | 6.05 fm, 21.08 MeV | $44\hbar$ | $4\hbar$ | $\approx 30\hbar$ | 49.63 MeV |
| $74.1 \pm 1.0$ | 1193 mb | 6.05 fm, 21.08 MeV | $46\hbar$ | $4\hbar$ | $\approx 31\hbar$ | 49.63 MeV |
| $79.5 \pm 0.9$ | 1190 mb | 6.05 fm, 21.08 MeV | $47\hbar$ | $4\hbar$ | $\approx 32\hbar$ | 49.63 MeV |
| $86.4 \pm 1.5$ | 1187 mb | 6.05 fm, 21.08 MeV | $49\hbar$ | $4\hbar$ | $\approx 34\hbar$ | 49.63 MeV |

$^{100}Rh$, $^{98}Rh$, $^{97}Ru$, $^{96}Tc$, $^{95}Tc$, $^{94}Tc$, and $^{93}Mo$ in the $^{12}C + ^{93}Nb$ system, $^{66}Ga$, $^{65}Ga$, $^{63}Zn$, and $^{61}Cu$ residues in the $^{12}C + ^{59}Co$ system, and $^{56}Ni$, $^{57}Ni$, $^{56}Co$, $^{57}Co$, and $^{58}Co$ residues in the $^{12}C + ^{52}Cr$ system produced in this energy range were considered. The cross-sections from a given reaction channel were determined separately from the observed intensities of all possible identified $\gamma$-rays, arising from the same radionuclide. The reported values are the weighted average of the various cross-section values obtained [39]. An analysis of experimentally measured EFs was made using the theoretical predictions of the PACE4 code [40,41], which is developed based on statistical Hauser-Feshback formalism followed by Monte Carlo simulations to determine the decay sequence of an excited compound nucleus.

The process of de-excitation of the excited nuclei was calculated using the PACE4 code which follows the correct procedure for angular momentum coupling at each stage of de-excitation. The angular momentum conservation is explicitly taken into account at each step. For any specific bombarding energy, the partial cross-section for CN formation at angular momentum $l$, $\sigma_l$, is

$$\sigma_l = \frac{\lambda^2}{4\pi}(2l + 1)T_l, \qquad (2)$$

where $\lambda$ is the reduced wave length and $T_l$, the transmission coefficient, is given by the expression

$$T_l = \left[1 + \exp\left(\frac{l - l_{\max}}{\Delta}\right)\right]^{-1}. \qquad (3)$$
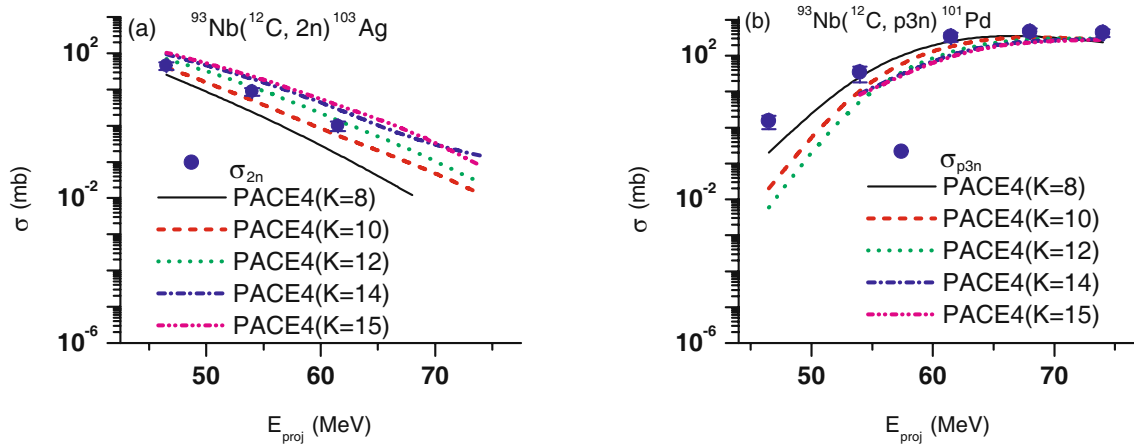
**Fig. 2.** (Color online) Experimentally measured and theoretically calculated EFs for residues $^{103}$Ag and $^{101}$Pd, populated via the CF channels of ($^{12}$C, 2n) and ($^{12}$C, p3n) in the $^{12}$C+$^{93}$Nb system within the energy range $\approx$ 45–75 MeV. The solid and broken curves represent the theoretical predictions of the PACE4 statistical model code at different values of $K$ ($K = 8$, 10, 12, 14 and 15), and the solid circles represent the measured cross-sections.

$\Delta$ is a diffuseness parameter and $l_{max}$, the maximum amount of $l$ detained by total fusion cross-section, is determined by

$$\sigma_F = \sum \sigma_l. \qquad (4)$$

The transmission coefficients for the light particles emission (n, p, and $\alpha$) during the de-excitation were determined using the optical model calculations [42–44]. In this calculation the input fusion cross-section was calculated using the Bass formula [45] (the values of Bass fusion cross-sections used in the present systems are given in tables 7–9). The evaporation cross-section was then determined by two other parameters: 1) the ratio of level densities at the saddle point and at the ground state, 2) the height of the fission barrier (which depends on the total spin). In these calculations, the de-excitation process, which used 100000 de-excitation cascades, was followed by a Monte Carlo procedure. And the statistical errors in the maxima of the EFs for all (measurable) residues populated in the interactions of the $^{12}$C projectile with the $^{93}$Nb, $^{59}$Co, and $^{52}$Cr targets were less than 5%. Transmission coefficients for light particles (n, p, and $\alpha$) evaporation were obtained during the first step of de-excitation by a full optical model calculation. Angular momentum projections were calculated at each stage of de-excitation, enabling the determination of the angular distribution of the emitted particles. Three parameters were involved in determining the various level densities needed for the calculations: the "little-$a$" parameter involved in particle evaporation calculation, the ratio $a_f/a$ of the little-$a$ parameter at the saddle point and ground-state deformations, and $B_f$, the fission barrier, which is taken to be equal to the rotating liquid drop fission barrier. In the description of $\gamma$-ray competitions, emission of $E1$, $E2$, $M1$, and $M2$ $\gamma$-rays are involved and $\gamma$-ray strength for different transitions, are taken from the systematic default values. The $\gamma$-decay intensities in Weisskopf units were $E1 = 0.000014$, $M1 = 0.10000$, $E2 = 5.900000$, $M2 = 0.000880$ for

$^{12}$C $+ ^{93}$Nb system and $E1 = 0.000080$, $M1 = 0.025000$, $E2 = 4.800000$, $M2 = 0.019500$ for $^{12}$C $+ ^{59}$Co and $^{12}$C $+ ^{52}$Cr systems. In this code the level density parameter $a$, which largely affects the equilibrium state components of cross-section is calculated from the expression $a = A/K$ MeV$^{-1}$, where $A$ is the nucleon number of a compound system and $K$ is an adjustable constant, which may be varied to match the experimental data. The experimentally measured EFs were compared with PACE4 predictions for different level density parameter values for representative evaporation residues in the $^{12}$C $+ ^{93}$Nb system produced only via the CF processes. For the evaporation residues $^{103}$Ag and $^{101}$Pd, the value of $K$ was varied to match the experimental data ($K$ values of 8, 10, 12, 14 and 15 were used) and the results are displayed in fig. 2. In tables 7–9 the most important input parameters used to perform the PACE4 code calculations are listed.

### 3.1 $^{12}$C $+ ^{93}$Nb system

The measured EFs along with theoretical predictions obtained using the PACE4 code for representative residues populated via non–$\alpha$-emitting channels, ($^{12}$C, 2n) and ($^{12}$C, p3n) are shown in fig. 2. In these sets of channels, there is no likelihood of ICF reactions, and therefore, these sets of channels are populated only by CF.

As can be seen from fig. 2 the calculated EFs corresponding to the level density parameter $K = 10$ in general reproduced satisfactorily experimentally measured EFs for the residues $^{103}$Ag and $^{101}$Pd produced in the CF reactions of the $^{12}$C projectile with the target, $^{93}$Nb.

The fact that the measured fusion cross-sections for non–$\alpha$-emitting (*non-$\alpha$-emit*) channels in the representative system, $^{12}$C $+ ^{93}$Nb, could be reproduced satisfactorily by PACE4 predictions, gives confidence in the input parameters chosen to fit the EFs of all (measurable) $\alpha$-emitting channels considered in the present systems.
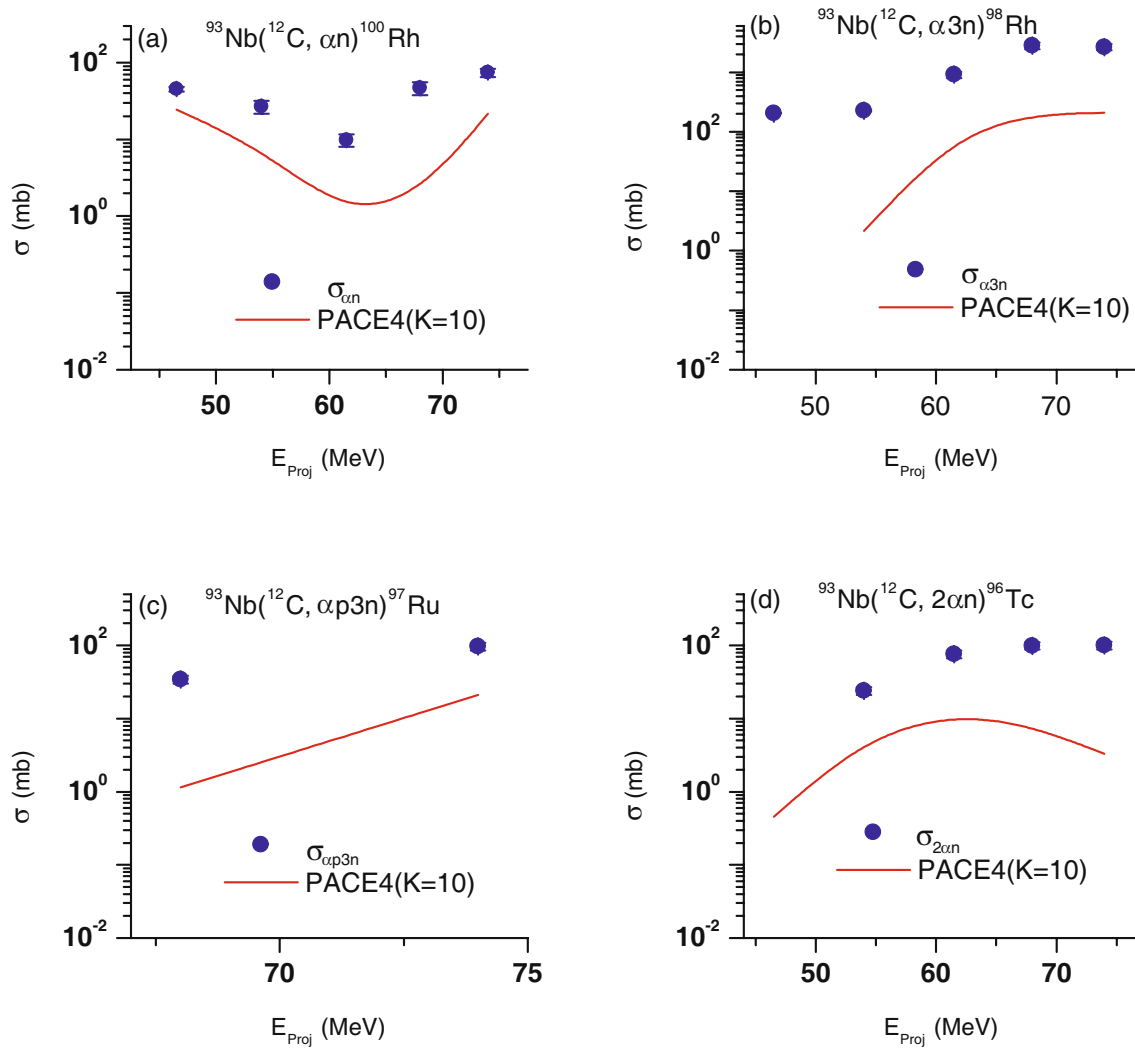
**Fig. 3.** (Color online) Experimentally measured and theoretically calculated EFs for $^{100}$Rh, $^{98}$Rh, $^{97}$Ru, and $^{96}$Tc residues in the interaction of the $^{12}$C + $^{93}$Nb system. The curves represent the PACE4 predictions with $K = 10$ and solid circles represent the experimental data.

It may also be observed from fig. 2 that the theoretical values obtained for different $K$ values, where $K > 10$, are mostly similar or differ very slightly.

It may, however, be pointed out that a value of $K > 10$ may give rise to an anomalous effect in respect of particle multiplicity, and compound nucleus temperature [46].

In the present work all calculations and analysis were performed consistently using $K = 10$, for all $\alpha$-emitting channels.

The EFs for seven radio-nuclides $^{100}$Rh, $^{98}$Rh, $^{97}$Ru, $^{96}$Tc, $^{95}$Tc, $^{94}$Tc, and $^{93}$Mo populated via $\alpha$-emitting channels in the interaction of $^{12}$C with $^{93}$Nb within the energy rage $\approx 45$–75 MeV are shown in figs. 3 and 4. The reaction products $^{100}$Rh, $^{98}$Rh and $^{97}$Ru may be formed via CF and /or ICF of $^{12}$C with $^{93}$Nb. In the case of CF, composite system $^{105}$Ag* is formed, which may then decay by the emission of $\alpha n$, $\alpha 3n$, or $\alpha p3n$ leaving $^{100}$Rh, $^{98}$Rh, and $^{97}$Ru residues, respectively. The same residues may also be populated via ICF, by $^{12}$C-nucleus breaking-

up (in the nuclear field of the target) into its fragments *viz.* $^{8}$Be and $\alpha$-particle. One of the fragments, $^{8}$Be, fuses with $^{93}$Nb, forming an incompletely fused composite system $^{101}$Rh*, which may then decay by emission of one neutron, forming $^{100}$Rh, three neutrons, forming $^{98}$Rh or one proton and three neutrons, forming $^{97}$Ru.

The residues $^{96}$Tc, $^{95}$Tc, and $^{94}$Tc may be formed via complete and/or incomplete fusion of $^{12}$C with $^{93}$Nb. In case of CF of $^{12}$C, a composite system of $^{105}$Ag* is formed, from which evaporation of one $\alpha$-particle and one, two or three neutrons takes place leaving behind $^{96}$Tc, $^{95}$Tc, and $^{94}$Tc residues. The same residues may also be populated via ICF $^{12}$C ion breaks in to $\alpha + {}^{8}$Be $(\alpha + \alpha)$ and $\alpha$ fuses with the target leaving $2\alpha$-paricles as spectators. The excited nucleus $^{97}$Tc*, may subsequently decay by emission of one neutron forming $^{96}$Tc, two neutrons forming $^{95}$Tc, or three neutrons forming $^{94}$Tc.

Similarly the residue $^{93}$Mo may also be formed by CF and/or ICF reactions as:
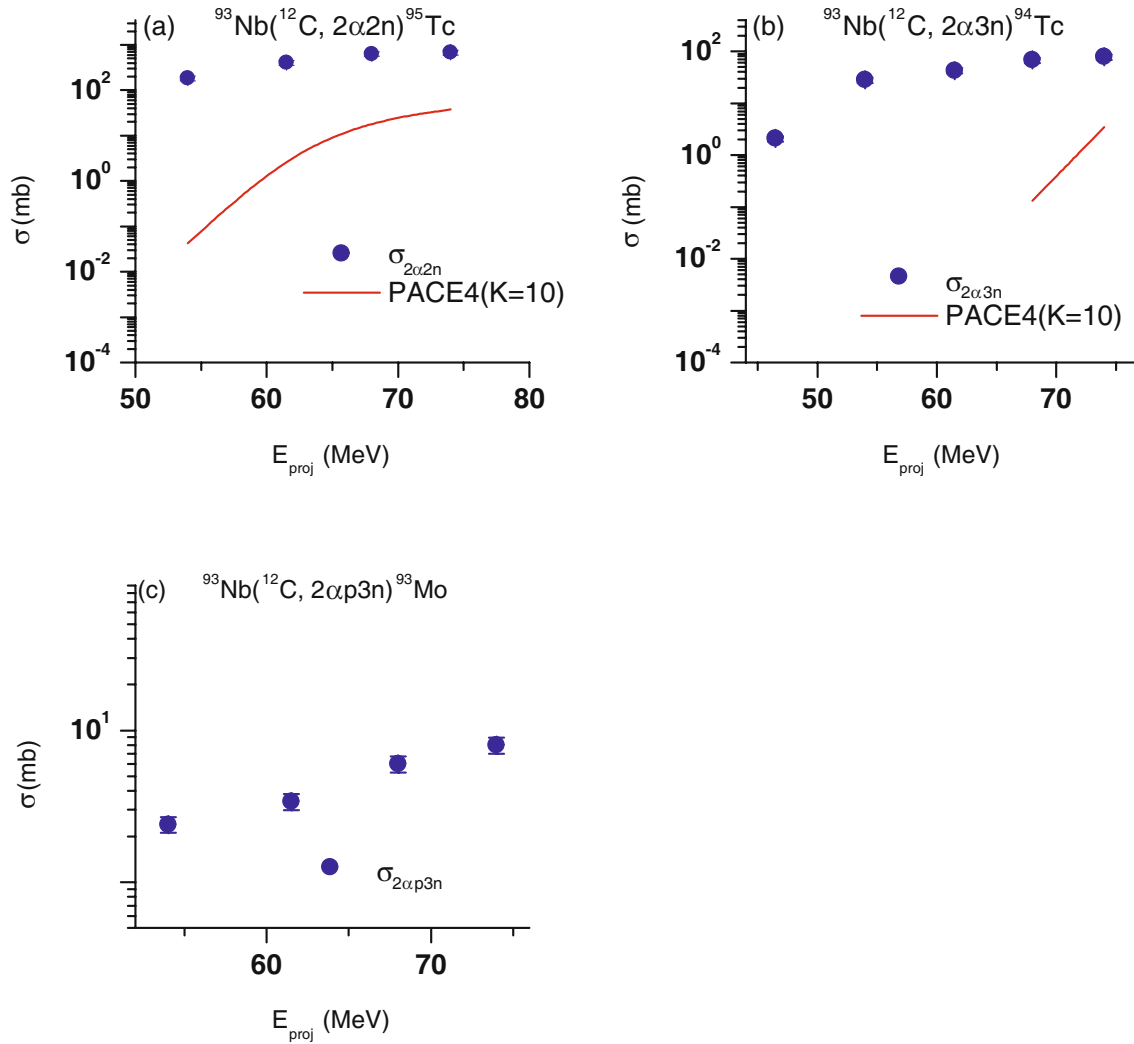
**Fig. 4.** (Color online) Experimentally measured and theoretically calculated EFs for $^{95}$Tc, $^{94}$Tc and $^{93}$Mo residues in the interaction of the $^{12}$C + $^{93}$Nb system. Explanation of symbols and curves are the same as fig. 3.

– Complete fusion of $^{12}$C, *i.e.*,

$$^{12}C + {}^{93}Nb \rightarrow [{}^{105}Ag]^* \rightarrow {}^{93}Mo + 2\alpha p3n.$$

– Incomplete fusion of $^{12}$C, *i.e.*,

$$^{12}C(\alpha + {}^{8}Be(\alpha + \alpha)) + {}^{93}Nb \rightarrow 2\alpha + [{}^{97}Tc]^* \rightarrow$$
$$^{93}Mo + p3n + 2\alpha \quad (2\alpha \text{ as spectators}).$$
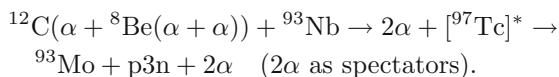
It may be observed from figs. 3 and 4 that the predicted theoretical values of cross-sections of the $\alpha$-emitting channels are found to be lower than that of the experimental data. Since ICF is not taken into consideration in PACE4, the observed enhancement may be credited to the contribution coming from ICF processes.

For $^{93}$Mo residue the theoretical values are negligible in this energy region, not shown in fig. 4(c).

## 3.2 $^{12}$C + $^{59}$Co system

The measured EFs along with theoretical predictions of PACE4 for $^{66}$Ga, $^{65}$Ga, $^{63}$Zn, and $^{61}$Cu residues populated in the fusion of the projectile $^{12}$C with the target, $^{59}$Co within the energy range of $\approx 60$–$80\,\text{MeV}$ are shown in fig. 5. In these residues, there is likelihood of ICF and, therefore, they may be populated by CF and/or ICF processes.

In $^{12}$C + $^{59}$Co system the production of these residues (via ICF) leading to $\alpha$ emissions channels may be explained in terms of the breakup of $^{12}$C ion into $\alpha + {}^{8}$Be and the fusion of $^{8}$Be fuses with $^{59}$Co to form an incompletely fused composite system, $^{67}$Ga$^*$ leaving $\alpha$-particle as spectator.

The residues $^{66}$Ga and $^{65}$Ga are expected to be populated following the emission of one or two neutrons from the composite nucleus $^{67}$Ga$^*$.
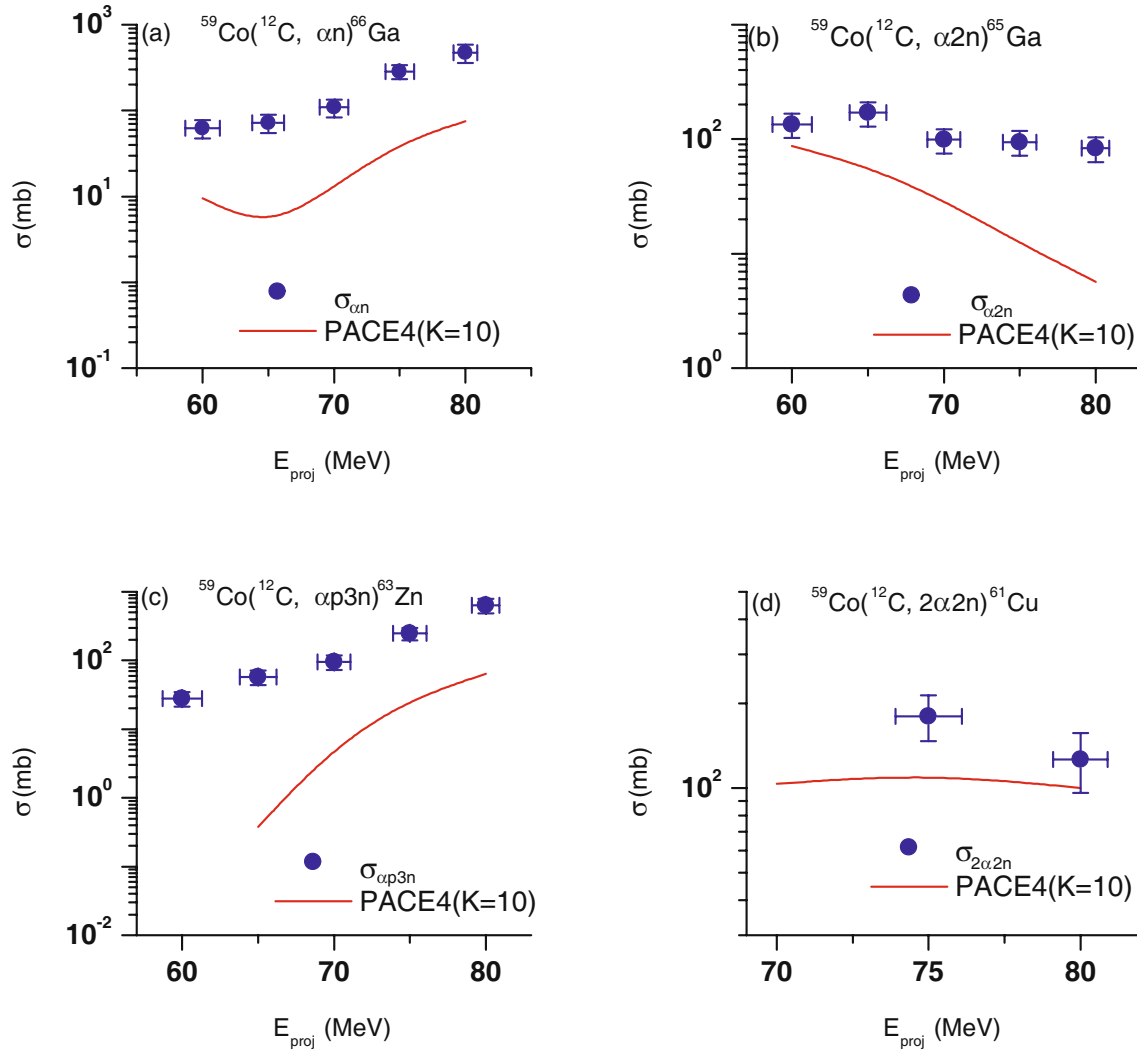
**Fig. 5.** (Color online) Experimentally measured and theoretically calculated EFs for $^{66}$Ga, $^{65}$Ga, $^{63}$Zn, and $^{61}$Cu residues populated in the interaction of the $^{12}$C $+$ $^{59}$Co system. The symbols represent the experimental data and curves represent PACE4 predictions with $K = 10$.

As such, the evaporation residues $^{66}$Ga and $^{65}$Ga may not only be populated by ICF but also via CF of the projectile leading to the formation of $^{71}$As$^*$, which may then decay by the emission of $\alpha$n and $\alpha$2n. The CF component calculated by PACE4 code is displayed in fig. 5(a)-(b) by solid lines.

As can be seen from these figures, the measured productions cross-section exhibit a significant enhancement compared to the theoretical predictions, which may be credited to the ICF processes.

The residue, $^{63}$Zn may also be formed by CF and/or ICF processes as:

– Complete fusion of $^{12}$C, *i.e.*,

$$^{12}\text{C} + {}^{59}\text{Co} \rightarrow [{}^{71}\text{As}]^* \rightarrow {}^{63}\text{Zn} + \alpha\text{p3n}.$$

– Incomplete fusion of $^{12}$C, *i.e.*,

$$^{12}\text{C}(^{8}\text{Be} + \alpha) + {}^{59}\text{Co} \rightarrow \alpha + [{}^{67}\text{Ga}]^* \rightarrow$$
$$^{63}\text{Zn} + \text{p3n} + \alpha, \quad (\alpha \text{ as a spectator}).$$
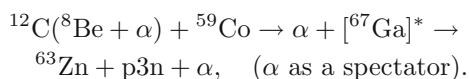
Similarly, the residue, $^{61}$Cu, may be populated through CF and/or ICF processes as:

– Complete fusion of $^{12}$C, *i.e.*,

$$^{12}\text{C} + {}^{59}\text{Co} \rightarrow [{}^{71}\text{As}]^* \rightarrow {}^{61}\text{Cu} + 2\alpha\text{2n}.$$

– Incomplete fusion of $^{12}$C, *i.e.*,

$$^{12}\text{C}(\alpha + \alpha + \alpha) + {}^{59}\text{Co} \rightarrow 2\alpha + [{}^{63}\text{Cu}]^* \rightarrow$$
$$^{61}\text{Cu} + 2\text{n} + 2\alpha, \quad (2\alpha \text{ as spectators}).$$
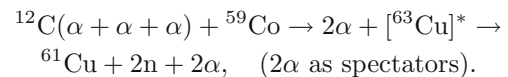
Figure 5(c)-(d) shows the measured and the calculated EFs for $^{63}$Zn and $^{61}$Cu residues. As can also be seen from these figures the measured cross-sections show a significant enhancement, especially at lower energy points, which may also be attributed to large ICF reactions.
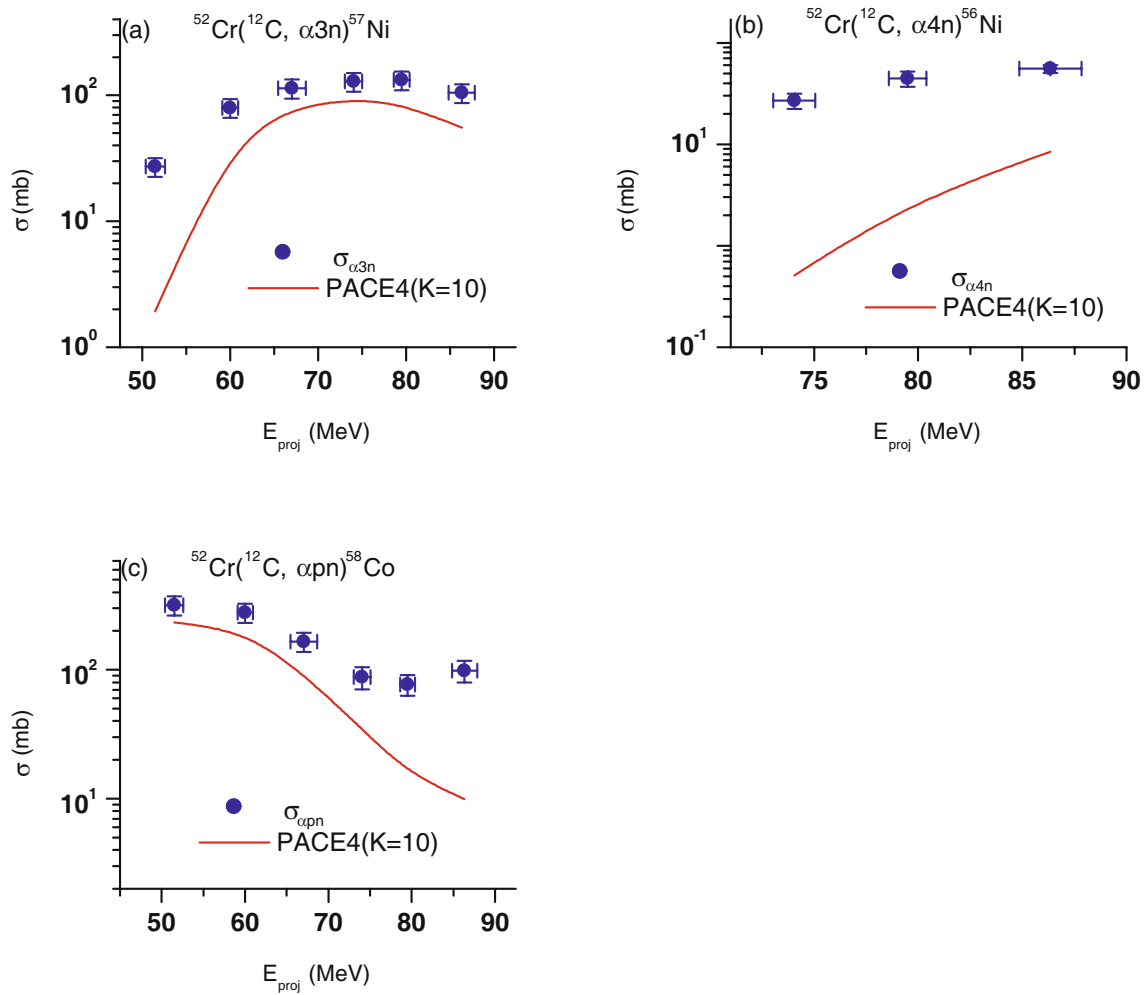
**Fig. 6.** (Color online) Experimentally measured and theoretically calculated EFs for $^{57}$Ni, $^{56}$Ni, and $^{58}$Co residues populated via ($^{12}$C, $\alpha xn$) ($x = 3, 4$) and ($^{12}$C, $\alpha pn$) channels in the $^{12}$C + $^{52}$Cr system. The curves represent the PACE4 predictions for $K = 10$ and solid circles represent the experimental data.
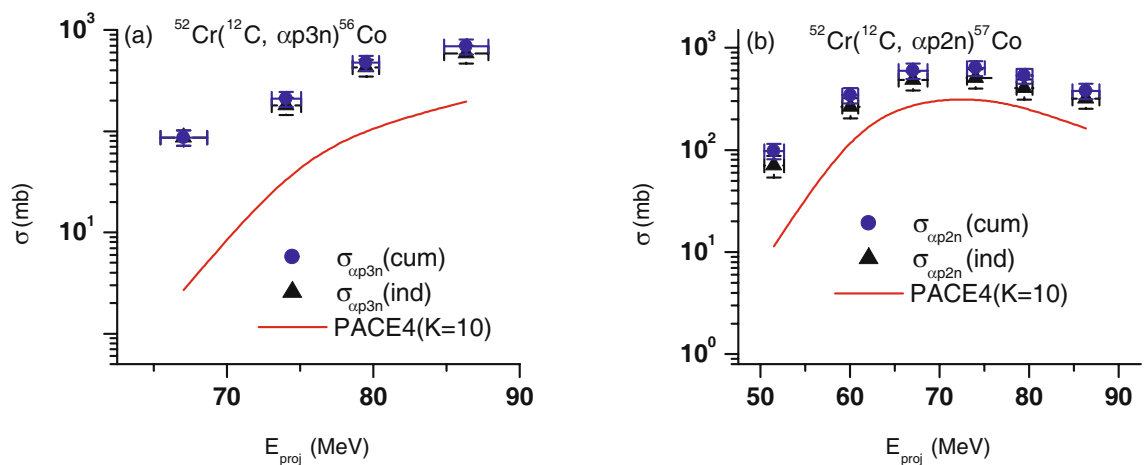


**Fig. 7.** (Color online) Experimentally measured and theoretically calculated EFs for $^{56}$Co and $^{57}$Co residues populated in the interaction of the $^{12}$C + $^{52}$Cr system. The independent and cumulative yields of these residues are also displayed. The solid triangles represent the deduced independent cross-sections and the remaining symbols representations are the same as in fig. 6.

### 3.3 $^{12}$C + $^{52}$Cr system

The measured EFs along with theoretical predictions obtained from PACE4 for residues $^{56}$Ni, $^{57}$Ni, $^{56}$Co, $^{57}$Co and $^{58}$Co populated via ($^{12}$C, $\alpha 4n$), ($^{12}$C, $\alpha 3n$), ($^{12}$C, $\alpha pn$), ($^{12}$C, $\alpha p2n$), and ($^{12}$C, $\alpha p3n$) channels, are shown in figs .6 and 7.

The residues $^{56}$Ni and $^{57}$Ni may be formed via complete and/or ICF of $^{12}$C with $^{52}$Cr. In case of CF of $^{12}$C, a composite system of $^{64}$Zn$^*$ is formed, from which evaporation of one $\alpha$-particle and three or four neutrons takes place leaving behind $^{56}$Ni and $^{57}$Ni residues. The same residues may also be populated via ICF: the $^{12}$C ion breaks into $\alpha + ^{8}$Be and $^{8}$Be fuses with the target leaving $\alpha$-particle as spectator. The excited nucleus, $^{60}$Ni$^*$, may subsequently decay by the emission of three neutrons forming $^{57}$Ni and four neutrons forming $^{56}$Ni.

Similarly, the residues $^{56}$Co, $^{57}$Co and $^{58}$Co may also be populated through CF and/or ICF process. In case of CF of $^{12}$C with $^{52}$Cr, a composite system of $^{64}$Zn$^*$ is formed, which may subsequently decay by emission of $\alpha pn$-, $\alpha p2n$- and $\alpha p3n$-particles forming $^{58}$Co, $^{57}$Co, and $^{56}$Co, respectively.

As a result of ICF of $^{12}$C with the target, a composite system of $^{60}$Ni$^*$ is formed leaving $\alpha$-particle as spectator. $^{60}$Ni$^*$ may subsequently decay by the emission of pn, p2n, and p3n particles followed by the formation of $^{56}$Co, $^{57}$Co and $^{58}$Co residues, respectively.

Further, note that residues $^{57}$Co and $^{56}$Co may also be populated by the decay of higher charge isobaric precursor (HCIP) decay as shown below:

$$^{12}\text{C} + {}^{52}\text{Cr} \rightarrow [^{64}\text{Zn}]^* \rightarrow [^{57}\text{Ni}]^* + \alpha 3n;$$
$$[^{57}\text{Ni}]^* \rightarrow {}^{57}\text{Co} + \text{EC}/\beta^+.$$
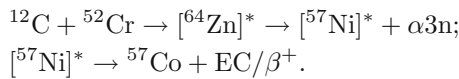
And the population of $^{56}$Co residue may also be formed by a HCIP decay of the type:

$$^{12}\text{C} + {}^{52}\text{Cr} \rightarrow [^{64}\text{Zn}]^* \rightarrow [^{56}\text{Ni}]^* + \alpha 4n;$$
$$[^{56}\text{Ni}]^* \rightarrow {}^{56}\text{Co} + \text{EC}/\beta^+.$$
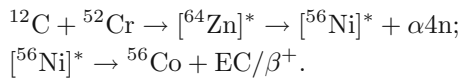
Since the precursors, $^{56}$Ni and $^{57}$Ni, have a relatively shorter half-life of $\approx 6\,$d and $\approx 1.5\,$d compared to the $\approx 77.7\,$d and $\approx 271.8\,$d half-life of the corresponding daughter nuclei, $^{56}$Co and $^{57}$Co, the measured activity of the residues, $^{56}$Co and $^{57}$Co, has contributions from their respective precursors. An attempt was made to separate out the contribution of the HCIP decay from the cumulative activity of $^{56}$Co and $^{57}$Co.

The cumulative cross-section, $\sigma_{cuml}$ of a given residue is the sum of i) its independent production cross-section, $\sigma_{ind}$, deduced from the measured cumulative cross-section using the relationship in eq. (5) and ii) cross-section for independent production of its precursor $\sigma_{prec}$ multiplied by a numerical coefficient $F_{prec}$ [47],

$$\sigma_{cuml} = \sigma_{ind} + F_{prec}\sigma_{prec}. \tag{5}$$

The value of $F_{prec}$ depends on the branching ratio $B_{prec}$ for HCIP decay to the residue and is given by

$$F_{prec} = B_{prec}\frac{T_{ind}}{T_{ind} - T_{prec}}, \tag{6}$$

where, $T_{ind}$ and $T_{prec}$ are the half-lives of the residue and the precursor, respectively. As such, the cumulative cross-section is given by

$$\sigma_{cuml} = \sigma_{ind} + B_{prec}\frac{T_{ind}}{T_{ind} - T_{prec}}\sigma_{prec}. \tag{7}$$

The values of branching ratios and half-lives required for obtaining the $B_{prec}$ coefficients are taken from *Tables of Nuclear Wallet Card* [48]. Using the above formulation in the present case, the cumulative yield, $\sigma_{cuml}$ and the deduced independent yield, $\sigma_{ind}$, for $^{56}$Co and $^{57}$Co are related by the equations

$$\sigma_{cuml}(^{56}\text{Co}) = \sigma_{ind}(^{56}\text{Co}) + 1.085\sigma_{prec}(^{56}\text{Ni}), \tag{8}$$

$$\sigma_{cuml}(^{57}\text{Co}) = \sigma_{ind}(^{57}\text{Co}) + 1.006\sigma_{prec}(^{57}\text{Ni}). \tag{9}$$

Here, $\sigma_{prec}(^{56}\text{Ni})$ and $\sigma_{prec}(^{57}\text{Ni})$ are the independent yield of their respective precursors. As such, the HCIP contribution of $^{56}$Co and $^{57}$Co at different energies was subtracted from the cumulative yields to separate out the independent yields. The measured cumulative cross-sections, $\sigma_{cuml}$ as well as independent cross-sections, $\sigma_{ind}$ for $^{56}$Co and $^{57}$Co residues deduced in this way are given in table 6 and are also plotted in fig. 7.

As can be seen from figs. 6 and 7 the calculated EFs corresponding to the level density parameter $K = 10$ in general did not reproduce experimentally measured EFs for the residues $^{56}$Ni, $^{57}$Ni, $^{56}$Co, $^{57}$Co and $^{58}$Co produced in the interaction of the $^{12}$C projectile with the target, $^{52}$Cr. Since PACE4 does not take ICF into account, the enhancement in the experimentally measured EFs may be attributed to the contribution of ICFs of the type

$$^{12}\text{C}(^{12}\text{C} \rightarrow \alpha + {}^{8}\text{Be}) + {}^{52}\text{Cr} \rightarrow {}^{8}\text{Be} + {}^{52}\text{Cr} + \alpha$$
$$\rightarrow \alpha + [^{60}\text{Ni}]^*, \quad (\alpha \text{ as a spectator}).$$
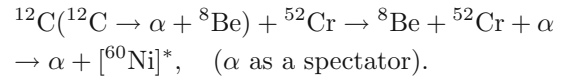
It may also be observed from fig. 7 that the contributions of the precursors $^{56}$Ni and $^{57}$Ni, to the production of the $^{56}$Co and $^{57}$Co nuclides, respectively, are relatively small. It may, however, be pointed out that the cumulative and independent yields of $^{56}$Co and $^{57}$Co reaction products are almost the same in the measured energy range of the $^{12}$C + $^{52}$Cr system.

It has already been mentioned that all $\alpha$-emitting channels identified in the present systems are expected to have significant contributions from the ICF process.

As such the ICF cross-section, $\sigma_{ICF}$, for an individual $\alpha$-emitting ($\alpha$-emit) channel was deduced by determining the difference between the HCIP decay corrected experimentally ($exp$) measured cross-section, $\sigma_{\alpha-emit}(exp)$, and theoretically ($theo$) calculated cross-section, $\sigma_{\alpha-emit}(theo)$, at different projectile energy points, as suggested by Gomes *et al.* [32]. The deduced ICF cross-section $\sigma_{ICF}$ for individual residues are plotted in fig. 8 along with the sum of all ICF $\Sigma\sigma_{ICF}$ as a function of projectile energy for the present systems.

It is clearly seen from this figure that ICF production cross-sections, $\Sigma\sigma_{ICF}$ increase significantly with increase in projectile energy, which is expected as the breakup probability of the incident ion significantly increases with projectile energy.
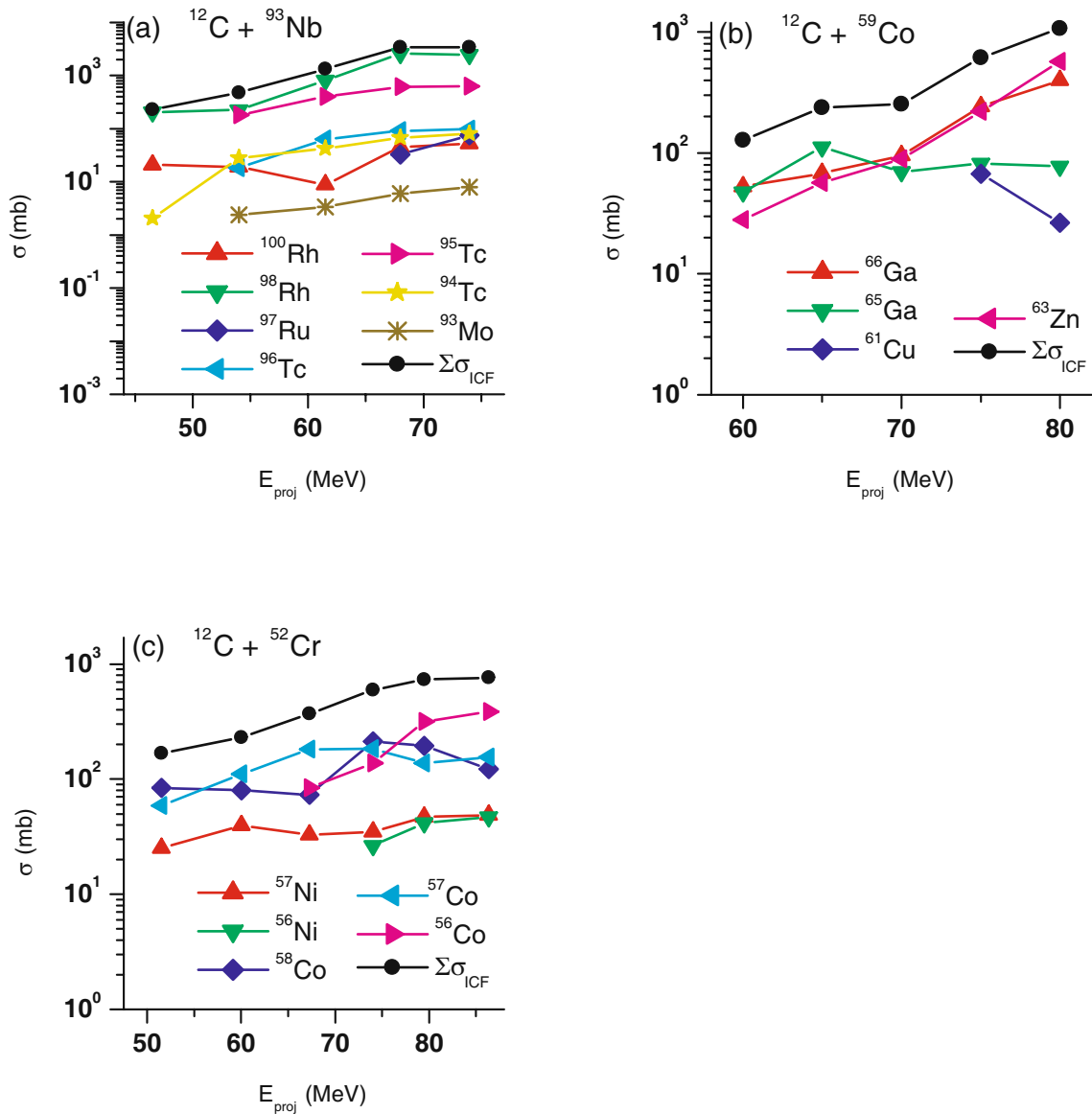
**Fig. 8.** (Color online) Deduced ICF contribution for individual residues along with the total sum of ICF cross-sections, $\Sigma\sigma_{ICF}$ for (a) the $^{12}C + {}^{93}Nb$, (b) the $^{12}C + {}^{59}Co$, and (c) the $^{12}C + {}^{52}Cr$ systems. The lines connecting the data points are just to guide the eyes.

## 4 Incomplete fusion fraction

In fig. 9(a)–(c), the HCIP decay corrected total ICF cross-sections, $\Sigma\sigma_{ICF}$, and total CF cross-sections, $\Sigma\sigma_{CF}$ ($\Sigma\sigma_{CF} = \Sigma\sigma_{non-\alpha-emit}(exp) + \Sigma\sigma_{\alpha-emit}(theo)$), were plotted along with the total fusion cross-section, $\sigma_{TF}$ ($\sigma_{TF} = \Sigma\sigma_{CF} + \Sigma\sigma_{ICF}$) for all (measurable) evaporation residues populated in the $^{12}C + {}^{93}Nb$, $^{12}C + {}^{59}Co$, and $^{12}C + {}^{52}Cr$ systems.

As can be observed from these figures the CF components have significant contributions up to $\approx 62.9$ MeV, $\approx 73.5$ MeV, and $\approx 75.5$ MeV for the $^{12}C + {}^{93}Nb$, $^{12}C + {}^{59}Co$, and $^{12}C + {}^{52}Cr$ systems, respectively, while ICF's influence seems to start at these points. For the $^{12}C + {}^{93}Nb$ system at $\approx 62.9$ MeV (*i.e.* where ICF starts to influence) the relative contribution of ICF is about

$\approx 54.2\%$ of the total fusion cross-section and increases to $\approx 69.3\%$ at $\approx 74$ MeV (the highest energy point).

Similarly, for the $^{12}C + {}^{59}Co$ and $^{12}C + {}^{52}Cr$ systems the contribution increases from $\approx 49.3\%$ and $\approx 49.6\%$ of the total fusion cross-section at the starting point to $\approx 67.1\%$ and $\approx 57.9\%$ at their respective highest energy point.

Further, it is clearly seen from these figures that the separation between the plots for $\Sigma\sigma_{CF}$ and $\sigma_{TF}$ increases significantly with an increase in the projectile energy, which indicates that the ICF contribution becomes larger at relatively higher energy points in the present systems. This may be due to an increase in the probability of projectile fragmentation into $\alpha$-clusters ($^8Be(\alpha+\alpha)+\alpha$) as the projectile energy increases. It may, however, be pointed out that the difference between the plots of $\Sigma\sigma_{CF}$ and
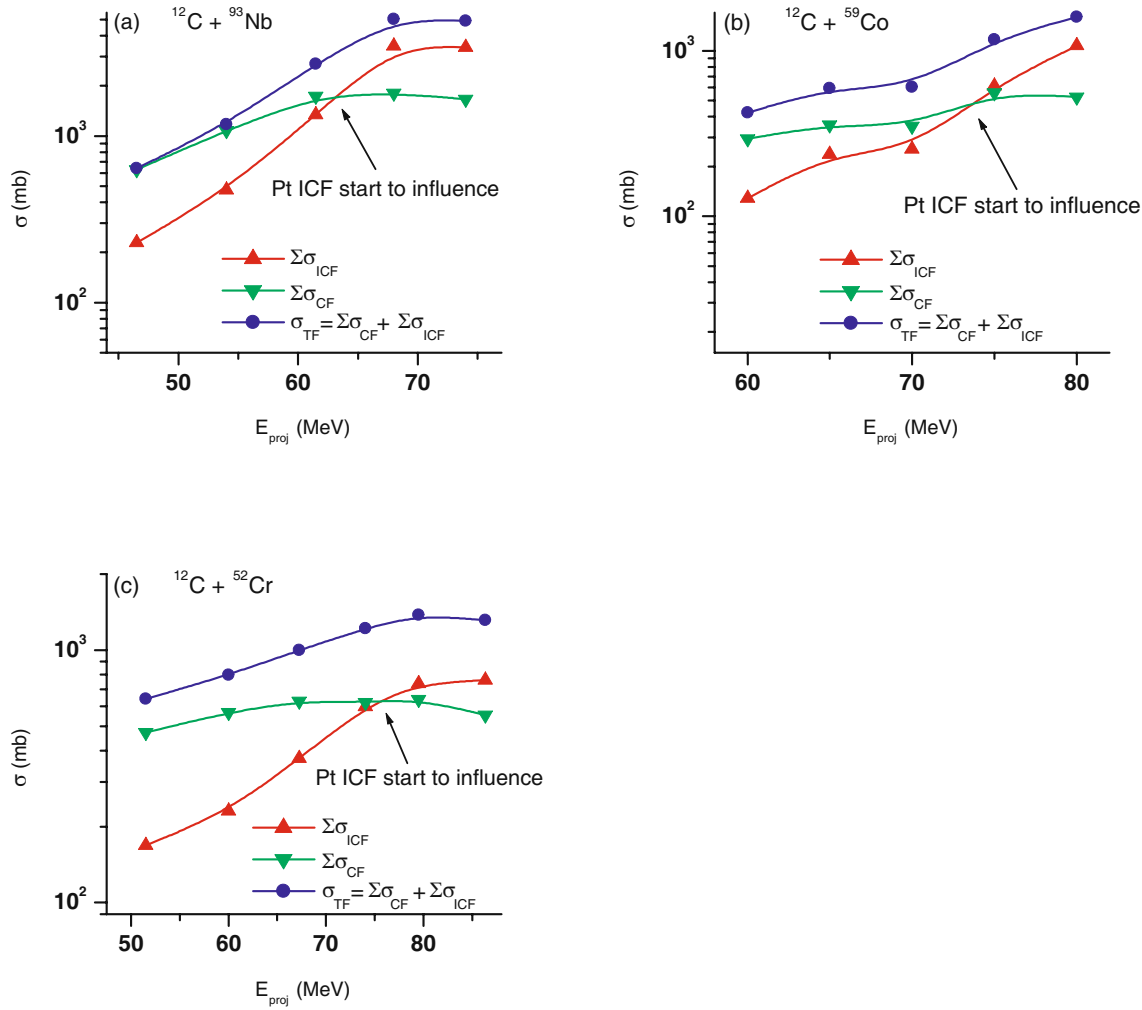
**Fig. 9.** (Color online) The total sum of the measured, $\sigma_{TF}$ and the total sum of the CF cross-sections, $\Sigma\sigma_{CF}$ along with the total sum of ICF cross-sections, $\Sigma\sigma_{ICF}$ at at various energies for (a) the $^{12}$C + $^{52}$Cr, (b) $^{12}$C + $^{59}$Co, and (c) $^{12}$C + $^{93}$Nb systems. The curves connecting the data points are just to guide the eyes.

$\sigma_{TF}$ is more for the $^{12}$C + $^{93}$Nb system as compared to the $^{12}$C + $^{59}$Co and $^{12}$C + $^{52}$Cr systems.

Moreover, to investigate the dependence of ICF contribution on energy, the percentage fraction of the ICF process, $P_{ICF} = \frac{\Sigma\sigma_{ICF}}{\sigma_{TF}} \cdot 100\%$, was deduced for the $^{12}$C + $^{93}$Nb ($V_{CB} \approx 36$ MeV), $^{12}$C + $^{59}$Co ($V_{CB} \approx 26$ MeV), and $^{12}$C + $^{52}$Cr ($V_{CB} \approx 24$ MeV) systems.

Figure 10(a) displays the graph of $P_{ICF}$ as a function of normalized projectile energy, $E_{proj}/V_{CB}$.

As can be seen from this figure, $P_{ICF}$ increases with the increase in projectile energy for presently studied systems.

An attempt was also made to estimate the energy dependence of $P_{ICF}$ for $^{16}$O + $^{169}$Tm and $^{16}$O + $^{103}$Rh systems available in the literature [5,8] and the results are shown in fig. 10(b). As can be seen from this figure, the ICF fraction for these systems also increases with the increase in projectile energy.

However, as it may be seen from fig. 10 at higher energy points the fraction of ICF approaches to nearly the same value or differ slightly, in general. This may be because of the fact that as the beam energy increases; the effect of Coulomb barriers goes on diminishing.

To study the dependence of $P_{ICF}$ on the entrance channel mass-asymmetry, the percentage fraction of ICF, $P_{ICF}$, were plotted in fig. 11 as a function of normalized relative velocity, $\nu_{rel}/c$, for the presently studied systems, along with two other systems available in the literature [5,8] where

$$\nu_{rel} = \left[ \frac{2(E_{c.m.} - V_{CB})}{\mu} \right]^{1/2}, \qquad (10)$$

$\mu$ is the reduced mass of the system, $E_{c.m.}$ is the center-of-mass energy. The data are plotted against normalized relative velocity, $\nu_{rel}/c$, which takes in to account the difference in $V_{CB}$ between the respective two sets of systems. As can be seen from these figures, in general, the values of $P_{ICF}$ in $^{12}$C + $^{93}$Nb are higher than that of $^{12}$C + $^{59}$Co
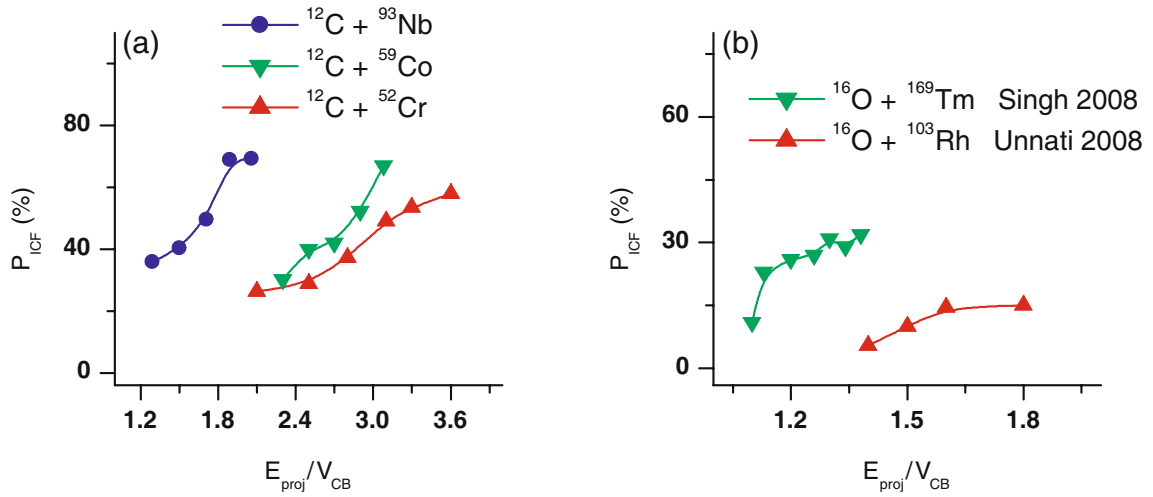
**Fig. 10.** (Color online) The percentage ICF fraction as a function of normalized projectile energy for (a) the present systems along with (b) values of systems available in the literature of Singh 2008 [5] and Unnati 2008 [8]. The curves connecting the data points are to guide the eyes.
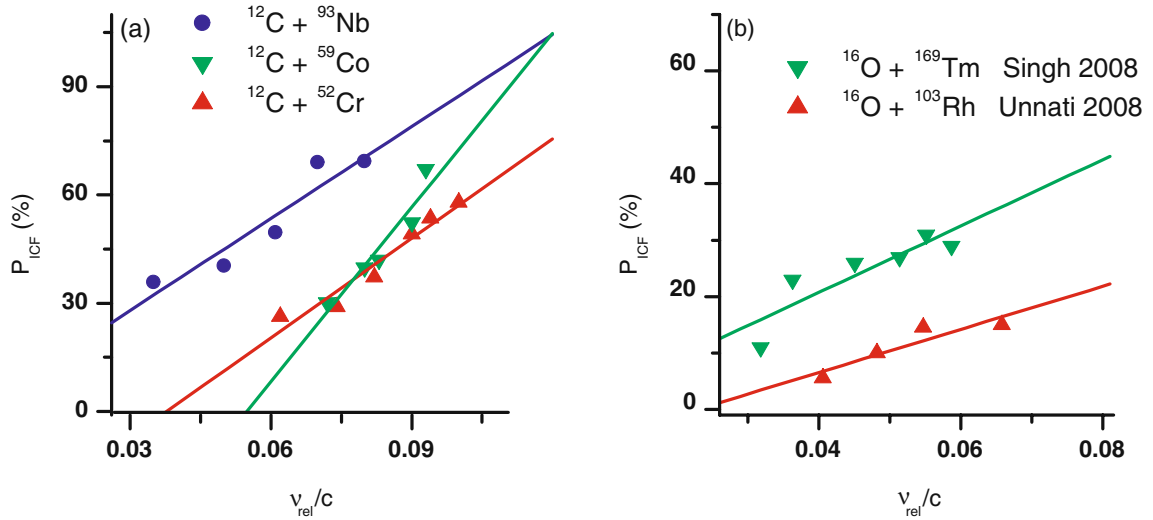


**Fig. 11.** (Color online) ICF fraction as a function of normalized relative velocity for (a) $^{12}C + ^{93}Nb$, $^{12}C + ^{59}Co$, and $^{12}C + ^{52}Cr$ systems along with (b) $^{16}O + ^{169}Tm$ and $^{16}O + ^{103}Rh$ systems available in the literature of Singh 2008 [5] and Unnati 2008 [8].

and $^{12}C + ^{52}Cr$ systems in the respective energy ranges. In similar way, the values of $P_{ICF}$ in $^{16}O + ^{169}Tm$ system are higher than that of the observed values for $^{16}O + ^{103}Rh$ system.

The difference between the two pairs of systems can be seen quite clearly, which may indicate the sensitiveness of $P_{ICF}$ on entrance channel mass asymmetry ($\frac{A_T}{A_T + A_P}$)

It may further, however, be pointed out that the probability of ICF is more in mass-asymmetric system than relatively mass-symmetric system, which supplement the systematic presented by Morgenstern *et al.* [49].

## 5 Summary and conclusions

We measured most of the present results in order to investigate the influence of ICF on CF of different evap-

oration residues produced in the present work. EFs for seven radio-nuclides: $^{100}Rh$, $^{98}Rh$, $^{97}Ru$, $^{96}Tc$, $^{95}Tc$, $^{94}Tc$, and $^{93}Mo$ produced in a $^{12}C + ^{93}Nb$ system: four radio-nuclides: $^{66}Ga$, $^{65}Ga$, $^{63}Zn$, and $^{61}Cu$ produced in a $^{12}C + ^{59}Co$ system; and five radio-nuclides: $^{57}Ni$, $^{56}Ni$, $^{58}Co$, $^{57}Co$, and $^{56}Co$ produced in a $^{12}C + ^{52}Cr$ system via complete and/or incomplete fusion in the beam energy ranging from $\approx 45$ MeV to 87 MeV were measured.

The measured EFs were compared with calculations done using the PACE4 statistical model code.

The measured CF cross-sections for the representative non–$\alpha$-emitting channels in the $^{12}C + ^{93}Nb$ system revealed an agreement with the values predicted by PACE4.

For $\alpha$-emitting channels, the measured cross-sections after correcting the HCIP contribution (if any) were significantly higher than the values predicted by PACE4.

This enhancement in the measured cross-sections is attributable to the ICF reactions.

For a $^{12}$C + $^{93}$Nb system, the approximate ICF fraction was found to be less than 54.2% at the starting point ($\approx 62.9$ MeV), but at the highest energy point ($\approx 74$ MeV) it reached approximately 69.3% of the total fusion cross-section. However, the ICF fraction was found to be approximately 49.3% and 49.6% at the starting point of ICF influence and $\approx 67.1\%$ and $\approx 57.9\%$ at the highest energy point for $^{12}$C + $^{59}$Co and $^{12}$C + $^{52}$Cr systems, respectively.

It may, however, be pointed out that ICF fraction is also found to be more in mass-asymmetric systems than mass-symmetric systems. The observation of high ICF fraction is attributable to the prompt breakup of the projectile into $\alpha$-clusters wherein the projectile, $^{12}$C, breaks up into $^8$Be + $^4$He and/or $^4$He + $^4$He + $^4$He leading to an ICF reaction. It was found that the probability of breakup increases with an increase in the incident projectile energy. Thus, it may be inferred that, in general, the ICF fraction is sensitive to the incident projectile energy and mass asymmetry of the entrance channel. It is found that the fraction of ICF increases significantly with increase in beam energy. This work's observations are supportive of Morgenstern systematic [49].

From the analysis of the relative yields of ICF products, it may be concluded that as well as CF, ICF is a process of great importance even at these energies. Thus, it is important that when predicting total reaction cross-sections, the contributions of ICF reactions are taken into consideration. Further, in the reactions of the present systems the sum of ICF cross-sections, $\Sigma\sigma_{ICF}$ were found to increase with energy. Moreover, to have a better insight into the relative contributions of ICF and CF reactions, more experiments using various projectile-target combinations at various energy ranges need to be carried out.

# References

1. F. Schussler, H. Nifenecker, B. Jakobsson, V. Kopijar, K. Soderstrom, S. Leray, C. Ngo, S. Souza, J.P. Bondrof, K. Sneppen, Nucl. Phys. A **584**, 704 (1995).
2. E. Gadioli, C. Brattari, M. Cavinato, E. Fabrici, E. Gadioli Erba, V. Allori, A. Di. Fillippo, S. Vailati, T.G. Stevens, S.H. Connell, J.P.F. Sellschop, F.M. Nortier, G.F. Steyn, C. Marchetta, Nucl. Phys. A **641**, 271 (1998).
3. Sunita Gupta, B.P. Singh, M.M. Musthafa, H.D. Bhadwaj, R. Prasad, Phys. Rev. C **61**, 64613 (2000).
4. D.R. Zolnowski, H. Yamada, S.E. Cala, A.C. Kahler, T.T. Sugihara, Phys. Rev. Lett. **41**, 92 (1978).
5. P.P. Singh, B.P. Singh, M.K. Sharma, Unnati, D.P. Singh, R. Prasad, R. Kumar, K.S. Golda, Phys. Rev. C **77**, 014607 (2008).
6. P.P. Singh, M.K. Sharma, Unnati, D.P. Singh, R. Kumar, K.S. Golda, B.P. Singh, R. Prasad, Eur. Phys. J. A **34**, 29 (2007).
7. D.J. Parker, J. Asher, T.W. Conlon, I. Naqib, Phys. Rev. C **30**, 143 (1984).
8. Unnati, P.P. Singh, D.P. Singh, M.K. Sharma, A. Yadav, R. Kumar, B.P. Singh, R. Prasad, Nucl. Phys. A **811**, 77 (2008).
9. S. Gupta, B.P. Singh, M.M. Musthafa, H.D. Bhardwaj, R. Prasad, Phys. Rev. C **61**, 064613 (2000).
10. Manoj Kumar Sharma, B.P. Singh, Sunita Gupta, M.M. Muthafa, H.D. Bhardwaj, R. Prasad, J. Phys. Soc. Jpn. **72**, 1917 (2003).
11. M.K. Sharma, Unnati, B.K. Sharma, B.P. Singh, H.D. Bhardwaj, R. Kumar, K.S. Golda, R. Prasad, Phys. Rev. C **70**, 044606 (2004).
12. M.K. Sharma, Unnati, B.P. Singh, R. Kumar, K.S. Golda, H.D. Bhardwaj, R. Prasad, Nucl. Phys. A **776**, 83 (2006).
13. E.A. Bakkum, P. Decowski, K.A. Griffioen, R.J. Meijer, R. Kamermans, Phys. Rev. C **39**, 2094 (1989).
14. J.H. Barker et al., Phys. Rev. Lett. **45**, 424 (1980).
15. D. Hojman, N. Wang, X. Wu, Z. Li, M. Liu, W. Scheid, Phys. Rev. C **74**, 044604 (2006).
16. H.C. Britt, A.R. Quinton, Phys. Rev. **124**, 877 (1961).
17. T. Inamura, M. Ishihara, T. Fakuda, T. Shimoda, H. Hiruta, Phys. Lett. B **68**, 51 (1977).
18. P.P. Singh et al., Phys. Sym. V **51**, 361 (2006).
19. T. Udagawa, T. Tamura, Phys. Rev. Lett. **45**, 1311 (1980).
20. J. Wilczynski, K. Siwek-Wilczynska, J. VanDriel, S. Gonggrijp, D.C.J.M. Hageman, R.V.F. Janssens, J. Lukasiak, R.H. Siemssen, S.Y. Van Der Werf, Nucl. Phys. A **373**, 109 (1982).
21. M. Blann, Phys. Rev. Lett. **27**, 337 (1971).
22. R. Weiner et al., Nucl. Phys. A **286**, 282 (1980).
23. J.P. Bondrof et al., Nucl. Phys. A **333**, 285 (1980).
24. V.I. Zagrebaev, Ann. Phys. (NY) **197**, 33 (1990).
25. H. Morgenstern, W. Bohne, W. Galster, D.G. Kovar, H. Lehr, Phys. Lett. B **113**, 463 (1982).
26. H. Morgenstern, W. Bohne, W. Galster, K. Grabisch, Z. Phys. A **324**, 443 (1986).
27. H. Fuchs, K. Mohring, Rep. Prog. Phys. **57**, 231 (1994).
28. I. Tserruya et al., Phys. Rev. Lett. **60**, 14 (1988).
29. D.J. Parker, J.J. Hogan, J. Asher, Phys. Rev. C **35**, 161 (1987).
30. Avinash Agarwal, I.A. Rizvi, Rakesh Kumar, B.K. Yogi, A.K. Chaubey, Int. J. Mod. Phys. E **17**, 393 (2008).
31. A.F. Kifle, B. Zelalem, A.K. Chaubey, Avinash Agarwal, I.A. Rizvi, Anjana Maheshwari, Tauseef Ahmed, Phys. Rev. C **84**, 024614 (2011).
32. P.E. Hodgson, E. Gadioli, E. Gadioli-Erba, *Introductory Nuclear Physics* (Oxford University Press, London, 1997) Chapt. 18.
33. P.R.S. Gomes et al., Phys. Lett. B **601**, 20 (2004).
34. J.F. Ziegler, *The Stopping Power and Range of Ion in Matter* (2006) SRIM-2006.
35. B. Wilken, A.T. Fitz, Nucl. Instrum. Methods **138**, 331 (1976).
36. FREEDOM Data acquisition and analysis software, designed to support accelerator based experiments at the IUAC, New Delhi, India.
37. E. Browne, R.B. Firestone, V.S. Shirley, *Table of Radioactive Isotopes* (Wiley, New York, 1986).

38. Rahbar Ali, D. Singh, M. Afzal Ansari, M.H. Rashid, R. Guni, S.K. Das, J. Phys. G: Nucl. Part. Phys. **37**, 115101 (2010).
39. S.F. Mughabghab, M. Divadeenam, N.E. Holden, *Neutron Cross-Sections*, Vol. **1**, Part A (Academic Press, New York, 1981) p. 89.
40. O.B. Tarasov, D. Bazin, Nucl. Instrum. Methods B **204**, 174 (2003).
41. A. Gavron, Phys. Rev. C **21**, 230 (1980).
42. J. Rapaport, V. Kulkarni, R.W. Finlay, Nucl. Phys. A **330**, 15 (1979).
43. F.G. Perey, Phys. Rev. **137**, 745 (1963).
44. J.R. Huizeya, G. Igo, Nucl. Phys. **29**, 462 (1962).
45. R. Bass, Nucl. Phys. A **231**, 45 (1974).
46. J.P. Lestone, Phys. Rev. C **53**, 2014 (1996).
47. M. Cavinato, E. Fabrici, E. Gadioli, E. Gadioli-Erba, P. Vergani, M. Crippa, G. Colombo, I. Redaelli, M. Ripamonti, Phys. Rev. C **52**, 2577 (1995).
48. J.K. Tuli, *Nuclear Wallet Card*, 6th edition (Brookhaven National Laboratory, Upton, New York, 2000).
49. H. Morgenstern, W. Bohne, W. Galster, K. Grabisch, A. Kyanowski, Phys. Rev. Lett. **52**, 1104 (1984).